The contribution of polar plumes to the fast solar wind

A. H. Gabriel[1], F. Bely-Dubau[2] and P. Lemaire[1]

gabriel@ias.fr

ABSTRACT

The Doppler dimming technique is used for the first time to study ultraviolet polar plumes in the height range 1.05 to 1.35 $R_\odot$, using observations from the spectrometer SUMER on SOHO. It is found that, contrary to a number of published suggestions, outflow velocities in the plumes *exceed* those in the interplume regions. Plume velocities are in excess of 60 km/s and are approximately constant throughout this height region. They tend to converge with the velocity of the accelerating interplume material at some height above our region of study. The analysis suggests that plume material makes a substantial contribution to the total line of sight, favouring either a "curtain" model for plumes or a chance alignment of a number of elementary cylindrical plumes. The intrinsic local density of plume material is some 20% to 50% in excess of the interplume regions. Estimation of the total mass outflow indicates that approximately half of the fast solar wind at 1.1 $R_\odot$ arises from plumes, with the remainder from interplume material. This result validates the published electron temperature profile of David et al. for the fast wind onset, which had been questioned over the suggestion that the flow velocity might be negligible in solar plumes.

Subject headings: solar plumes, fast solar wind

1. Introduction

The solar plumes treated in this article are the radial, or near-radial bright rays, seen beyond the solar limb in the UV and XUV radiation characteristic of temperatures of around 1 MK. These plumes, observed within the height range 1.0 to 1.3 $R_\odot$, have been the subject of many studies since the launch of SOHO, in particular involving the instruments SUMER, CDS and EIT. Their association with structures formed at other heights and wavelengths has been discussed in numerous papers, but remains for the moment a matter of speculation. The UV features are normally seen within coronal holes at the solar limb, although one group claims also to detect them in low-latitude holes against the disk.

Since it is now widely accepted that coronal holes are the principal source regions for the fast solar wind, it becomes increasingly important to evaluate whether the plumes are a significant contribution to this outflow. During the minimum of solar activity, coronal holes are concentrated in the form of two large holes around the solar poles. Plumes which are observed in these favourable conditions are often referred to as polar plumes.

2. Plume studies

SOHO was launched during the solar minimum in December 1995 and the best observations of polar plumes were consequently recorded during the first two years of its life. DeForest et al. (1997) reported that the polar plumes observed by EIT are contiguous with plume-like rays seen in white light through Thomson scattering, using ground-based and space coronagraphs out to 15 $R_\odot$. They further claimed to identify their origins on the disk as small unipolar flux concentrations. DeForest et al. (2001a) later showed images claiming this correlation out to 30 $R_\odot$. The present work is limited to UV and XUV plumes out to 1.35 $R_\odot$, leaving until later the discussion of their relation to other

---

[1]Institut d'Astrophysique Spatiale, 91405 Orsay Cedex, France

[2]Observatoire de la Côte d'Azur, BP4229, 06304 Nice Cedex, Franc

observed plume-like features.

Efforts to determine the different physical properties of plumes and the intervening darker regions, referred to as interplume regions, have been made by several workers. Wilhelm et al. (1998) used spectroscopic line ratio diagnostics with SUMER to measure the density and temperature. They found the temperature of plumes to be slightly lower than interplume regions. They suggested that the principal outflow comes from the interplume region. This view has been supported by many workers, although there have been no measurements of the outflow rate in plumes at these heights, prior to the present work. Giordano et al. (2000) have used the UVCS instrument on SOHO at greater radial distances, in order to measure the outflow rate in plumes. They used the Doppler dimming technique, developed by the UVCS team (Noci et al. 1987) to interpret the observed intensity ratio of the oxygen VI multiplet at 1032 Å and 1038 Å. Their results suffered from large error bars, but claimed to show a significantly higher velocity in the interplume regions over the range 1.5 to 4 $R_\odot$. Patsourakos and Vial (2000) measured the flow rate at one point in an interplume region at 1.05 $R_\odot$, using SUMER.

A fundamental problem arises concerning the 3-dimensional structure of the plumes. Their appearance could suggest cylindrical structures, and many workers have tried to interpret them as such. However an alternative model has been discussed by some other workers. This so-called "curtain" model proposes that the plumes are thin sheet structures that become visible only when they are viewed edge-on. As the Sun rotates they would then appear and disappear, on a time scale of a few days, which corresponds quite well with their observed duration. The curtain model also offers a further possibility that the corona within holes has only a single component, so that plume and interplume regions are the same material, viewed parallel or perpendicular to the sheet.

An important early SOHO observation was designed to measure the variation with height of the electron temperature in a polar coronal hole (David et al. 1998). This showed that the temperature never exceeds 1.0 MK before it begins to fall off with height. This observation, using an observing sequence known as JOP 002, depended on the ratio of spectral lines from both SUMER and CDS.

Since the CDS line was in the short wavelength GIS channel, where the instrument is astigmatic, the analysis provided no spatial resolution in the E-W direction and therefore integrated over the plume and interplume regions. If the suggestion of Wilhelm et al. (1998) that the wind flows preferentially from the interplume regions were to be verified, this would compromise the radial temperature measurement. The observations could then be dominated by the more intense plume regions, which would not be the material responsible for the solar wind onset.

To resolve this question was a further important motivation in pursuing the present research, aimed at determining the flow velocity in the plume and interplume regions. The approach is to apply the Doppler dimming technique, developed originally for the higher altitude UVCS observations, to the lower height observed with the SUMER instrument. This lower height region poses additional problems, compared with the UVCS measurements normally made around 2 $R_\odot$ or above. As we will show later, at the lower flow velocities, the value of the local electron density has a stronger influence on the observed measurements. Furthermore, the SUMER instrument, not being a coronagraph, requires extreme precautions to correct for the scattered instrumental light due to the brighter disk, which can amount to more than 30% of the total signal in oxygen VI at 1.3 $R_\odot$.

3. Observations

A unique and valuable data set was recorded during the solar minimum on 1996 May 21, using the SOHO spacecraft with its roll attitude rotated by 90 deg from the normal position. This observation, known as JOP 002, examined the north polar coronal hole, with the objective of measuring the radial variation of electron temperature (David et al. 1998). The measurements used the intensity ratio between lines recorded by the CDS/GIS and SUMER spectrometers. They were averaged over the slit lengths in the E-W direction, since the astigmatic CDS/GIS system does not allow spatial resolution in this direction. In the present paper, we revisit the SUMER observations of this data set, to exploit the 2-dimensional format, thereby resolving the plume/interplume structures. The intensities of the components of
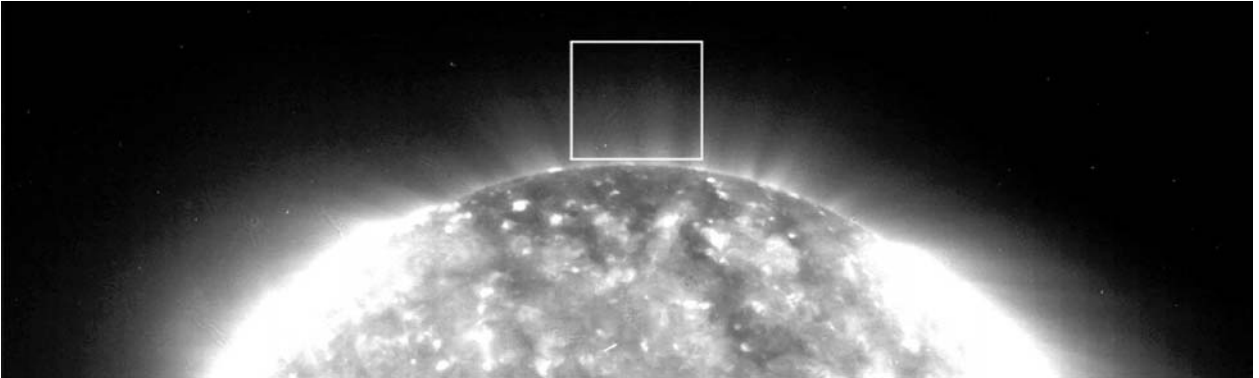
Fig. 1.— EIT image of the polar coronal hole, recorded at 171 Å. The superposed white rectangle shows the position of the coronal raster recorded by SUMER and shown in Fig 2.

the oxygen VI multiplet at 1032 Å and 1038 Å were measured. Their ratio varies normally between 2 and 4, depending on several quantities, but notably on the radial flow velocity in the corona, due to the Doppler dimming process (see Section 5.1).

The region studied is shown in Fig 1. This is an image recorded with the EIT instrument at 171 Å and shows clearly the presence of solar plumes. The principal region covered by the SUMER raster is indicated as the white rectangle, covering heights from 1.03 $R_\odot$ to 1.34 $R_\odot$. This is shown in Fig 2 in the emission from the 1032 Å oxygen VI line. We are fortunate in finding that this raster includes a region B with an intense plume, as well as a low intensity interplume region, A. The bright feature in the lower left corner is due to cold plasma and has no effect at heights of 1.1 $R_\odot$ and above. Also observed by SUMER was a region just inside, and crossing the solar limb. These data from the solar disk were used to determine and to correct for the instrument stray light contribution to the coronal signals. The SUMER spectroscopic channel was set throughout to record a wavelength range which includes the intense lines from oxygen VI near 1032 Å as well as the hydrogen Lyman β line at 1025 Å.

This data set is unique for several reasons. The possibility to observe the atmosphere above a coronal hole at the limb depends on the hole having a large extent in the line of sight, so as to avoid the tenuous low-density corona being contaminated by the brighter quiet Sun closed-field corona, in front or behind. Such conditions are only found for the
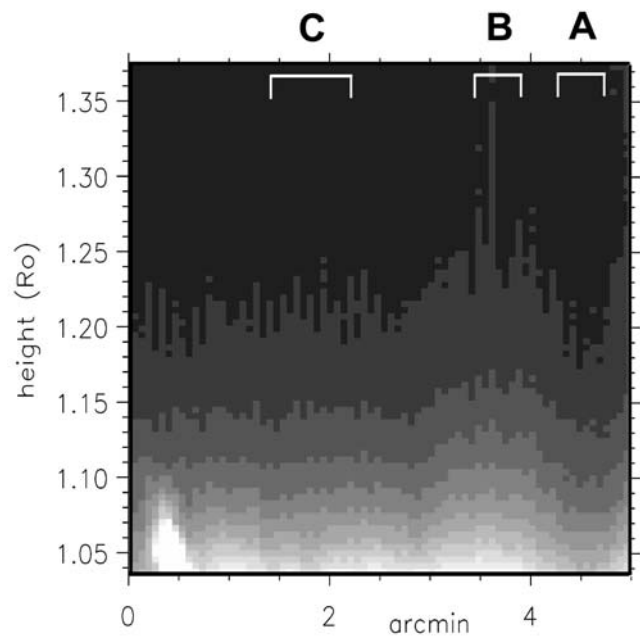

Fig. 2.— Raster recorded above the limb by SUMER in the wavelength 1032 Å.

large polar holes seen during the solar minimum. Four months following the recording of this data, SUMER suffered a loss of its rastering capability, which prohibits future recording of this type of 2-dimensional image from SOHO.

4.   Reduction and calibration of the data

SUMER corrections for flat field and image distortion were carried out using the available stan-

3

dard software package, which is capable also of performing an intensity calibration. The absolute intensity calibration of SUMER is a complex problem and it is unlikely that the value obtainable is reliable to better than 20%. However, we are able to carry out the majority of the measurements and interpretation for the present work, ignoring absolute intensities and dealing only with intensity ratios. These include the ratio of intensities in the oxygen VI multiplet, the ratio between the disk and above limb intensities and the ratio between coronal hole and non-hole intensities. It is essential for the present study to perform a precise correction for the instrumental stray light, since this can contribute substantially to the observed intensity around $1.3\,R_\odot$. It is necessary to evaluate and subtract the signal produced by the intense disk radiation at the same wavelengths, scattered from the primary telescope before entering the spectrometer slit. The technique used is that developed by David et al. (1997), based upon the prelaunch calibration data on the telescope mirror. The function is distributed as "cal_straylight.pro", included in the *ssw* software package. To apply the method, a model of the spatial distribution of the disk brightness is required. This medium resolution model requires high-resolution detailed representation only near the limb, within a few arcminutes of the coronal region being observed. To derive the model, the local darkening due to the presence of coronal holes near both poles needs to be taken into account. The technique was applied to images in the two oxygen VI lines, as well as to the Lyman β line.

4.1. Measurement of coronal hole contrast in oxygen VI seen against the disk

Except for a narrow annular ring near the extreme limb, the oxygen VI disk lines are optically thin in the line of sight. For a uniform Sun, this will lead to a disk brightness proportional to $1/cos\theta$, where θ is the angle between the viewing direction and the local normal to the surface, except at the extreme limb. In addition, the region around each pole will be darkened by some factor due to the modified atmospheric structure in the coronal holes. No satisfactory observational data exists in the literature for this darkening factor. To have good statistics and to average over the network fluctuations, this factor must be evalu-

ated over a reasonable area of a hole, seen against the disk. We have measured this hole contrast factor using a SUMER raster scan, taken two days before the primary observation. This covered a 240 arcsecond high band of the northern part of the Sun, including the northern limb and the coronal hole. Fig 3 shows the radial intensity trace, averaged over some 200 arcsecond in the E-W direction around the central meridian, with compensation for the limb curvature. The two dotted curves are best-fit $1/cos\theta$ profiles adjusted in amplitude for the hole and non-hole regions. This measurement yields a value for the hole of some $70 \pm 2\%$ of the non-hole brightness.
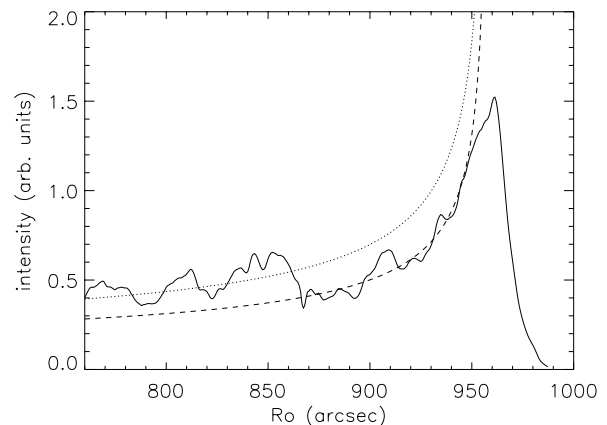

Fig. 3.— Radial scan on the disk in 1032 Å, showing the step in intensity at the edge of the polar coronal hole. The dotted curves are $1/cos\theta$ plots adjusted to fit the two regions.

4.2. Correction for SUMER telescope stray light

The first step is to construct an approximate brightness model of the total solar disk for use in the scattering code. Using the basic $1/cos\theta$ variation, together with the hole contrast measured above and the geometry of the hole boundary obtained from the EIT 171 Å image, a model of the relative brightness was constructed for the complete solar disk. This was normalised to the same calibration as our above-limb measurement, using the SUMER data recorded just inside of the limb as part of the primary observing sequence. The outermost 50 arcsecond of the disk model was re-

4

placed by the real observed data. In this way, the discontinuity in the $1/cos\theta$ function was avoided and the real brightness used in the narrow region at and just beyond the limb. This includes the annular region where the oxygen VI emission becomes slightly optically thick. Finally, the hole contrast as derived above was used to enhance the brightness of all of the disk falling outside of the polar holes. The same principle was adopted for the 1025 Å Lyman β line, but this is optically thick everywhere on the disk, so that the $1/cos\theta$ function was replaced by a constant value and no coronal holes were introduced. A part of this adopted model is shown in Fig 4 for the 1032 Å and 1025 Å lines.

Using these models of the disk brightness, and the scattering code following David et al. (1997), the contributions of disk stray light to the three lines, 1032 Å 1038 Å and 1025 Å were evaluated. The 1032 Å and 1025 Å lines are shown in Fig 5. Application of this method to the Lyman β line serves as a verification and fine calibration for the method. This line is not expected to have significant emission in the corona above 1.2 $R_\odot$, where the signal should be pure stray light. The fact that the calculated stray light is close to the signal observed at this height and with the same slope is a verification of the validity of the method. A small displacement on the log plot between the two, equivalent to around 6%, has been corrected, and the same factor applied to the two oxygen VI lines. This 6% is interpreted as the difference between the pre-launch calibration of stray light and the in-flight value.

It should be noted that previous workers (e.g. Hassler et al. (1997)), aiming to correct for instrumental scattering, have used the 1025 Å Lyman β line (or sometimes the carbon II line) in the corona as a measure of the stray light. However they have failed to take into account the very different disk brightness distribution for the optically thick Lyman β line and the optically thin emission being corrected. We calculate that this will produce an error factor in the stray light estimation of between 0.21 and 1.4, depending on which point on the disk (centre or limb) is chosen for normalising the disk/above-limb intensity ratio.
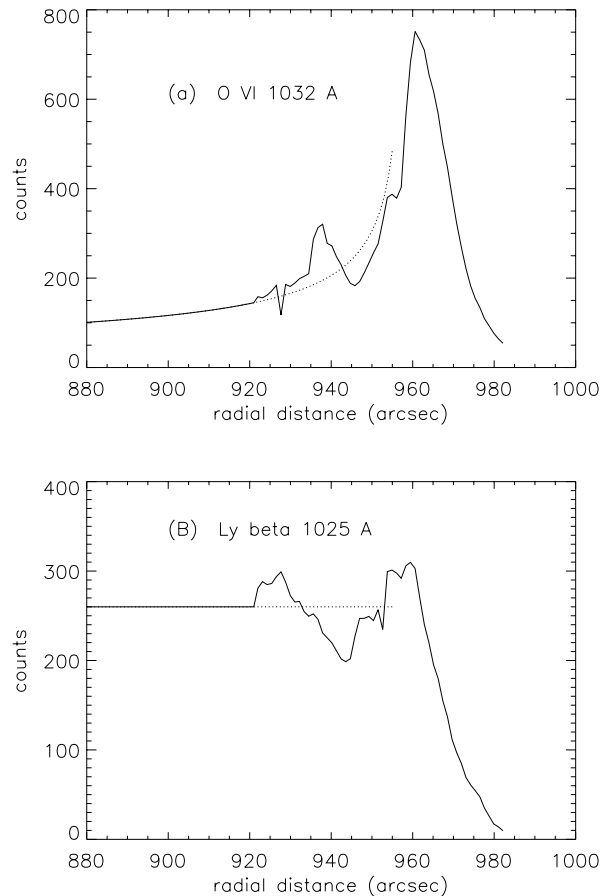

Fig. 4.— Radial profiles for disk models, used to compute the above-limb stray light contribution. Theoretical models below 920 arcsec are combined with real observations for the region near the limb. The near-limb portion of the theoretical models, shown as dotted lines, has not been used.

4.3. The corrected observational data

With the stray light contamination subtracted from the observed intensities, it is now possible to plot the intensity ratio for the multiplet against radial distance. This is shown in Fig 6 for two regions, the interplume region A and the strongest plume region B. Also shown in the figure as dotted lines are the limits of the variation that would obtain if there were a 10% error in the stray light correction. Evidently, such an error would be correlated between the two regions, in the sense that if the upper dotted curve were to apply for the re-
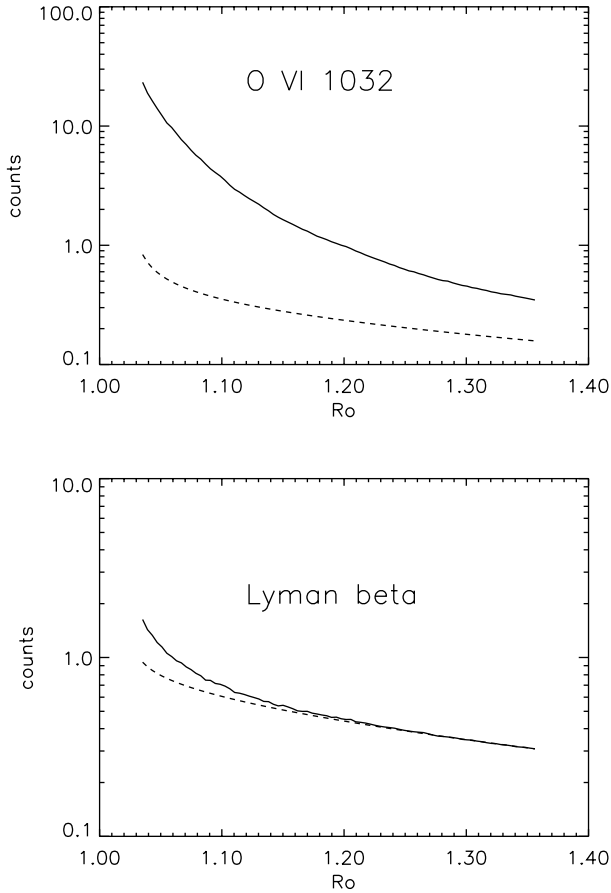
Fig. 5.— Above-limb observations in the lines 1032 Å and 1025 Å, shown as solid lines. The computed stray light contributions are shown as dashed lines.

gion A, then the upper curve would also apply for region B.

This figure shows the high quality of the multiplet ratio measurements, with small scatter of individual points. It indicates a clear significant difference between the plume and interplume multiplet ratios, which cannot be attributed to errors in the stray light correction.

To complete the presentation of the corrected observations, the brightness of the 1032 Å line is plotted in Fig 7 against E-W position, for different radial distances. It can be seen that the plume/interplume brightness ratio is nowhere higher than 1.6 and decreases with radial distance.
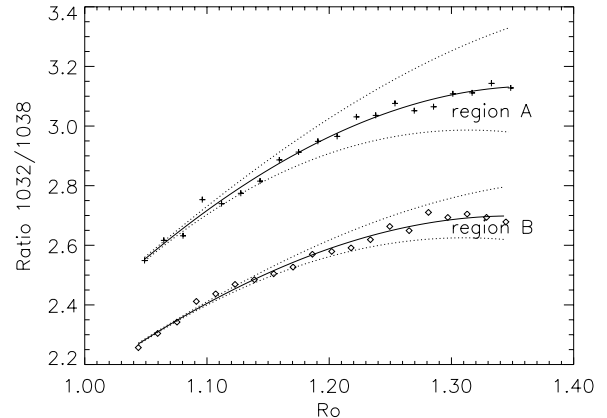

Fig. 6.— Observed coronal oxygen VI multiplet brightness ratio, after calibration and stray light correction is plotted here as a function of radial distance, for two of the regions indicated in Fig 2. The dotted curves show the limits obtained if there were an error of a factor 10% in the stray-light correction.

Before proceding to a detailed interpretation of the observed multiplet ratios, these observations tell us at once that a single component "curtain" mode of this atmosphere cannot be valid. If the plume and interplume represented merely two directions of viewing of similar curtains, then the multiplet ratios for the two regions would be the same, an interpretation excluded by the observations of Fig 6. This still leaves open the possibility that the plumes are due to a curtain structure, so long as this is imbedded in another medium, responsible for the interplume emission. We return to this discussion later.

5. Formation of the oxygen VI lines

The oxygen VI multiplet $2s - 2p$ $^2P_{3/2,1/2}$ at 1032 Å and 1038Å is formed mainly by electron impact excitation in the upper transition region, at around the temperature predicted by ionisation balance theory of 0.3 MK. Due to the tail of the equilibrium temperature distribution, the formation extends up to coronal temperatures, with significant coronal contribution to the intensity. The coronal contribution is predicted to be in the region of 10% to 30%, depending on the local coronal
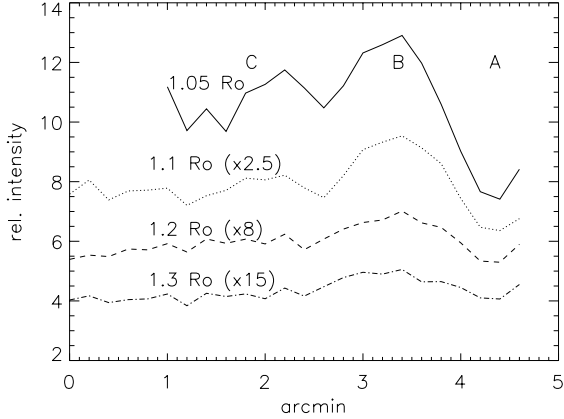
Fig. 7.— The intensity of the coronal oxygen VI 1032 Å line is here plotted against tangential position for four radial distances, in arbitrary units. The intensities have been scaled by the factors shown, for convenience of plotting.

temperature (hole or non-hole). The oxygen VI lines are excited mainly at lower heights by electron impact. The intensity I is then given by

$$I = N_{OVI} N_e C, \qquad (1)$$

where C is the collisional excitation rate coefficient and N_e the local electron density. If we use the subscripts 1 and 2 to indicate the lines 1032 Å and 1038 Å then the multiplet ratio M is given by

$$M = \frac{N_{OVI} N_e C_1}{N_{OVI} N_e C_2}, \qquad (2)$$

The ratio C_1/C_2 is determined by the statistical weights to be 2, so that the multiplet ratio M is also equal to 2. Since these lines are almost everywhere optically thin, the observed brightness ratio is then also 2, so long as impact excitation remains the dominant process. Just close to the limb, inside and outside, the path length in the line-of-sight becomes sufficient for some self-absorption, and the multiplet brightness ratio falls locally to around 1.5, as shown in Fig 8.

At increasing heights in the corona, as the density falls, the multiplet is also excited by photons coming from the transition region. We then have

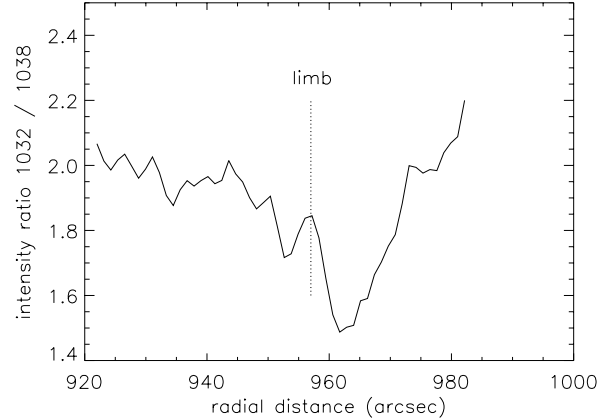$$M = \frac{N_{OVI} N_e C_1 + N_{OVI} \phi_1}{N_{OVI} N_e C_2 + N_{OVI} \phi_2}. \qquad (3)$$

Fig. 8.— Observations of the oxygen VI multiplet brightness ratio on the disk and crossing the limb. This shows how the disk value of 2.0 falls to 1.5 just above the limb due to self absorption and then increase towards the higher values in the corona shown in Fig 6.

The photo-excitation rates ϕ_1 and ϕ_2 depend on the intensity of the exciting radiation coming from the lower layers and also on the atomic absorption coefficients for the two levels. Each of these quantities is in the ratio of 2, so that the ratio ϕ_1/ϕ_2 is equal to 4. It can therefore be seen from Eq 3 that the multiplet ratio M will vary between 2 and 4, depending on whether the first terms are dominant (high N_e) or the second terms (low N_e). Beyond the limb, we therefore see a brightness ratio which increases through 2 towards higher values in the corona (see Fig 8).

5.1. Doppler dimming

A further process intervenes in determining the multiplet intensity ratio at increasing heights in the corona. This arises when the outflow velocity of the coronal plasma reduces the efficiency of the photo-excitation processes, due to a Doppler shift between the moving plasma and the excitation source. This diminution leads to a reduction in the values of ϕ, leading to a decrease in the multiplet intensity ratio, which then falls towards the pure impact excitation value of 2.0. The fact that the observed multiplet ratios increase between 1.1 and 1.3 R$_\odot$ (Fig 6) is the result of a conflict between the effect on one hand of a reducing density that

7

decreases the impact excited component and, on the other hand, the Doppler dimming effect that eventually reduces the photon excited component. At above 1.4 $R_\odot$, the ratio is expected to turn over and begin to fall, a tendency already apparent in Fig 6. We aim to interpret the oxygen VI multiplet ratio in the corona in terms of this Doppler dimming process, in order to provide the plasma outflow velocity in the plane of the sky, i.e. in a direction perpendicular to the direction of viewing. The theory was developed initially for the UVCS observations by Noci et al. (1987). We have revised and updated this theory, taking account of recent improvements in the atomic theory and knowledge of the solar disk emission but, more importantly, including the effect of limb brightening of the transition region exciting radiation. This last effect, included here for the first time in the Doppler dimming model, has an important contribution, which is larger when viewing closer to the limb. Our Doppler dimming model is described in more detail in the Appendix. A further discussion of Doppler dimming applied to oxygen VI in a polar coronal hole is presented by Raouafi et al. (2002), who treat many of the questions raised in the present study, but with the primary aim of interpreting the polarisation.

From Eq 3, we obtain that the local multiplet ratio

$$M = \frac{N_e C_1 + \phi_1}{N_e C_2 + \phi_2}, \qquad (4)$$

where ϕ is defined in the Appendix by Eq A1. M has a first order dependence on the local electron density N_e, and also on the outflow velocity v and the radial heliocentric distance of the line-of-sight R through ϕ. Fig 16 shows this variation for two radial distances, 1.1 and 1.3 $R_\odot$. There is also a much slower dependence on the electron temperature T_e and the ion thermal Doppler temperature T_i through $C_{1,2}$ and D (Eq A2). T_e has been set to 1.0 MK, following measurements made by David et al. (1998). In the case of the ion temperature, the sensitivity is even smaller (see Fig 16) and this has also been set to the same value of 1.0 MK. The possibility that T_i may be different in the parallel and perpendicular directions is ignored at the lower heights treated in the present paper, where UVCS studies show it to be a negligible effect.

Furthermore, the local volume emission rate for the 1032 Å line is given by

$$I = A(N_e^2 C_1 + N_e \phi_1). \qquad (5)$$

Here A is a constant, depending on the abundance and ionisation balance of oxygen.

6. The value of electron density

The Doppler dimming theory discussed above shows that it is impossible to derive a useful flow velocity unless a value can be assumed for the local electron density. This is even truer for the lines-of-sight closer to the limb used here. At greater distances, common in UVCS observations, the dependence on electron density is smaller and vanishes completely when the multiplet ratio M drops to a value near 2.0 (see Fig 16).

Unfortunately, the electron density was not measured simultaneously with the data-set used here. We are therefore obliged to adopt values based on observations of similar large polar coronal holes. In what follows in this Section, we refer only to the interplume regions, such as region A, which is assumed to occupy all of the line-of-sight, limited only by the curvature of the solar atmosphere. It is obvious that the plume regions, such as region B, are variable from plume to plume and that the line-of-sight extent is uncertain.

The question of the electron density at the coronal base of polar coronal holes has been debated at length, since it is an important parameter for the fast solar wind (see Wurz and Gabriel (1999)). It seems clear that there is a broad consistency between the measurements made on different occasions, so long as they use the same method of measurement. This suggests that the solar minimum polar coronal hole is a reproducible phenomenon and gives some reassurance to our approach of adopting standard values. However, the two different methods of measuring this quantity give notably different results and it is necessary to understand this difference.

The first method is the measurement of Thomson scattered photospheric radiation from free electrons, made during solar eclipses. This method would appear to involve a minimum of uncertain physical processes and yields a mean value of the electron density $\bar{N}$, after unfolding the line-of-sight. A review of results obtained over a number of observations is given by Koutchmy (1994), who

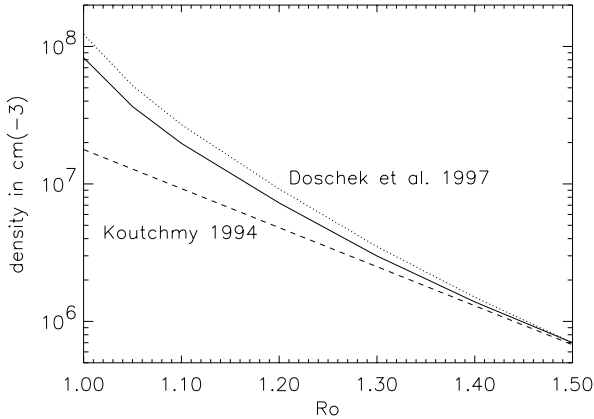cites values of around $2 \ 10^7 \ cm^{-3}$ at the coronal base.

Fig. 9.— Models of the electron density above a polar coronal hole. The dashed curve is a Thomson scattering mean value from Koutchmy (1994). The dotted curve is a local value from line ratio diagnostics (Doschek et al. 1997) and the full line is the modified local value adopted here (see Section 7).

The second method, adopted more recently, involves the ratio of two spectral line intensities from the ion silicon VIII, interpreted in terms of the excitation equilibrium of the ion excited states. This has been developed by Doschek et al. (1997) and Wilhelm et al. (1998), both using SUMER at periods not too far from the observations described here. They obtain values of around $1 \ 10^8 \ cm^{-3}$. Curves extracted from the two different measurements are reproduced in Fig 9 over the range 1.0 to 1.5 $R_\odot$. As this silicon VIII measurement depends on impact excitation processes, it measures the local value of the electron density N_e. Since both of these measurements appear to be reliable and reproducible, we make the assumption that they are both valid. If there exist inhomogeneities in the local density on scales too small to resolve, then these different values for mean density and local density can be consistent. If the inhomogeneities are assumed to be due to a simple "filling factor" effect, then this is of the order 15%, which could be considered a reasonable coronal filling factor. Fig 9 shows that the two curves converge at greater heights, indicating that the filling factor tends towards unity.

The local electron density N_e is the appropriate value for the Doppler dimming model. It represents the electron impact component, which has to be compared with the photo-excitation component. However, when later, in Section 7, we develop the equation of continuity for the expanding solar wind, then it is the mean electron density $\bar{N}$ that must be used.

7. Interpretation of the interplume structure (Region A)

For each height in the corona, the observed multiplet ratio M (Fig 16) can be expressed as a function of the outflow velocity and the local density, for which approximate values are given in Fig 9. A further inter-relation can be obtained from the equation of continuity of outflow mass. This involves the joint interpretation of data obtained from different heights in the corona. In this way, the approximate densities in Fig 9 can be adjusted to produce a self-consistent solution as a function of height.

Continuity implies that the velocity at a heliocentric distance R is given by

$$v_R = v_{1.1} \frac{\bar{N}_{1.1}}{\bar{N}_R} \left(\frac{1.1 R_\odot}{R}\right)^2 \frac{p_{1.1}}{p_R}, \qquad (6)$$

where $v_{1.1}$ is the outflow velocity defined at an arbitrary fixed height of 1.1 $R_\odot$, $\bar{N}$ is the mean electron density and p is a super-radial expansion factor. Following Munro and Jackson (1977), the expansion factor for a symmetric polar coronal hole is given by

$$p_R = \frac{p_{max} exp[(R - R_1)/\sigma] + p_1}{exp[(R - R_1)/\sigma] + 1}, \qquad (7)$$

where

$$p_1 = 1 - (p_{max} - 1) exp[(R_0 - R_1)/\sigma], \quad (8)$$

with $p_{max} = 7.26$, $R_1 = 1.31 \ R_\odot$, $\sigma = 0.51 \ R_\odot$, and $R_0 = R_\odot$.

Using these relations, together with the Koutchmy (1994) values for the mean density $\bar{N}$, and taking the Doschek et al. (1997) local density values N_e for the Doppler dimming effect, we obtain the set of dotted curves in Fig 10 for the calculated values of M, as a function of mass flow rate and

radial distance. The shorter dashed curve follows the observed M values for the region A, copied from Fig 6. A small adjustment to N_e, shown as the solid curve in Fig 9, results in a modification to the model, shown as the set of solid curves in Fig 10. In this way, an adjustment of the standard density profile is used to ensure agreement between the model and the observations at small radial distances, whilst the value of the mass flow rate has a more sensitive effect at larger radial distances. It can thus be shown that the Doschek densities are a better fit when adjusted in this way, and lead to a mass flow rate $v_{1.1}$ of 25 km/s. This requirement to modify the N_e values by a factor of less than 1.5 might be due to a difference between the coronal hole observed by Doschek et al. (1997) and that used in the present work. We note also the possibility of a contribution from errors in the atomic physics used to derive the Doschek line ratio diagnostic for density. For these forbidden lines in the ground configuration of silicon VIII, calculations are less reliable than for permitted transitions and must include also excitation by protons. We know also that proton kinetic temperatures can be somewhat higher than electron temperatures in these coronal regions.

The flow velocities derived by adopting the value for $v_{1.1}$ of 25 km/s are shown in Fig 11.

8. Analysis of the plume region B

With the interplume parameters determined, it is now possible to consider the plume regions, starting with the strongest plume, seen in region B. The effective line-of-sight of the interplume region A can be evaluated by assuming a spherical shell atmosphere, of thickness equal to the intensity scale-height. The tangential line-of-sight is then found to be of the order of 1 $R_\odot$. In region B, some fraction of the line of sight, say F, will be occupied by the plume, with the remaining $(1-F)$ occupied by interplume material. We have found no means of evaluating the line-of-sight depth of the plume, so that we keep F as a free parameter in the following analysis. For the often-assumed cylindrical plume, F will have a value of 0.1 or less. For a "curtain" model, F might be 0.5 or more. Assuming a particular value of F, and taking the observations of both the multiplet ratio M and the brightness enhancement of the 1032 Å line,
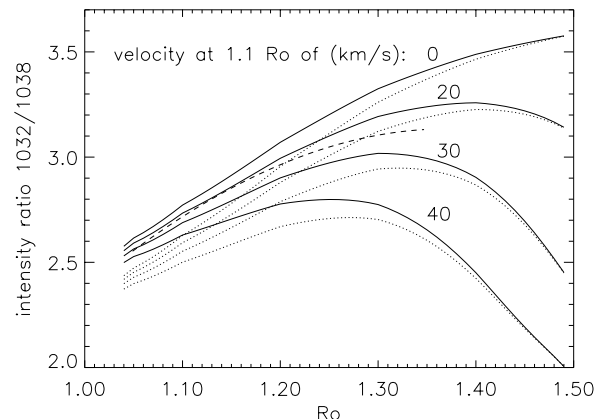

Fig. 10.— Curves showing the calculated variation of the interplume oxygen VI multiplet ratio against the radial height with, as a parameter, the mass flow rate, expressed in terms of the outflow velocity at 1.1 $R_\odot$. The dotted curve-set use the Doschek et al. (1997) local densities, whilst the full curves use the modified values shown in Fig 9. The observational values, copied from Fig 6, are shown as a dashed curve.
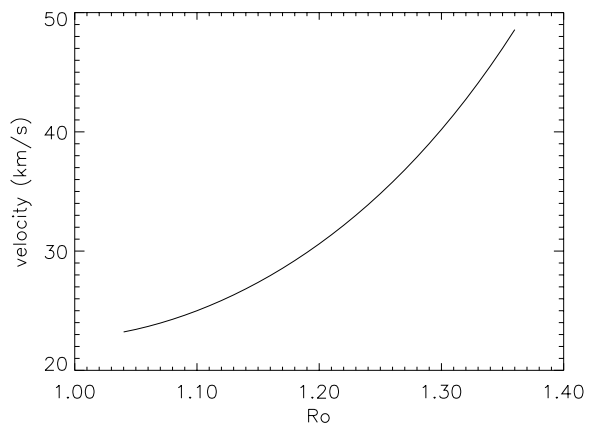

Fig. 11.— The interplume outflow velocity as a function of radial distance. This is based upon a constant mass flow model, with the flow rate determined by the fit of the observations to the set of models in Fig 10.

we can deduce the true local value of the plume multiplet ratio and the enhanced volume emission at 1032 Å of the plume material in the following

way.

We here use the subscripts A and B to denote observed quantities related to the interplume and plume regions viewed in the plane of the sky, and the subscripts i and p for the intrinsic volume emission in the interplume and plume plasma. For the observed multiplet ratio, we can write

$$M_B = \mathcal{M}(M_i, M_p, F) = \mathcal{F}_1(N_e, v, F). \quad (9)$$

Note that M_A is identical to M_i. For the observed brightness of the plume in 1032 Å, we take the ratio between the regions A and B

$$B_B/B_A = \frac{I_p F + I_i(1 - F)}{I_i} = \mathcal{F}_2(N_e, v, F). \quad (10)$$

In this way, the two observables can be expressed as functions of N_e, v and F.

Inversion of Eqs 9 and 10 is carried out by an iterative procedure, which is found to converge rapidly, passing around the loop only ~ 3 times. In this way, the flow velocity and the plume density enhancement can be found as functions of radial distance and, of course, the free parameter F. The derived quantities, v and N_{ep}/N_{ei} are shown plotted in Fig 12 and Fig 13. Note that here again the analysis uses only intensity ratios and never absolute intensities.
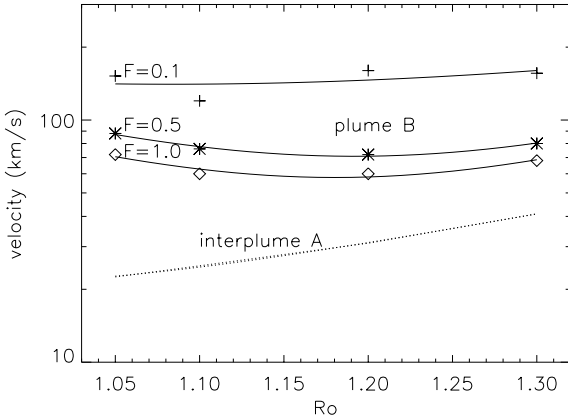

Fig. 12.— The derived outflow velocity for the plume B as a function of the radial distance and the line-of-sight parameter F. The interplume outflow from Fig 11 has been reproduced here as a dotted curve.
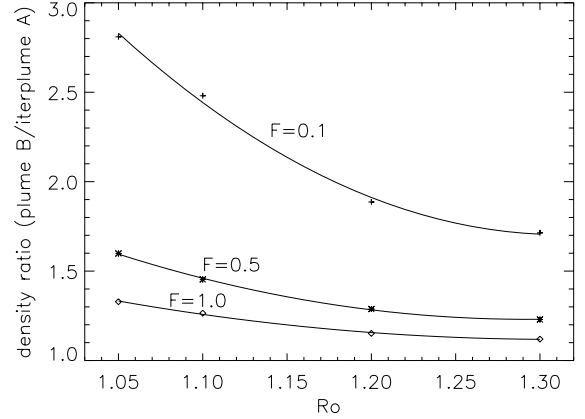

Fig. 13.— The density ratio plume/interplume is derived as a function of radial distance and the line-of-sight parameter F.

9. Summary of principal results

In Fig 12 is shown also for comparison the interplume outflow velocity, copied from Fig 11. It can be readily seen that for all values of F, the plume outflow is significantly higher than for the interplume. If we take the view that the values above 100 km/s are unreasonable high, then this gives preference to the larger values of F, which favours either a "curtain" model or several cylindrical plumes in the line of sight. However there is at present no objective reason for this choice. Within a reasonable error estimate, the plume curves are more or less horizontal, indicating an almost constant outflow velocity in the plume B. On the other hand, the interplume region has a lower velocity but accelerates, so that one can anticipate that the two will converge at a height somewhat above the limit of our observations at 1.35 R$_\odot$. Fig 13 shows the corresponding intrinsic density ratios between the plume B and the interplume. Evidently, for the smaller values of F, indicating the almost cylindrical plume, the density ratio would be higher. Here again, the density enhancement decreases with height, with a tendency to converge with the interplume at some greater distance.

11

10. Discussion

10.1. The weaker plumes (Region C)

Having interpreted the most intense plume of region B, we have to consider how to understand the several weaker plumes, marked as region C in Fig 2. One possibility is that they have the same physical properties as the plume B, but occupy less of the line of sight, that is to say, they have a smaller value of F. To test this idea, we plot in Fig 14 the theoretical prediction based on this assumption, in the form of the multiplet ratio M against the intensity of the 1032 Å line. The points plotted are the observational values for a horizontal cut across the different plume regions. We can deduce that the observations are broadly consistent with such a model. However, other models are also possible in which the region C represents plume material with lower density enhancements and higher values of F.
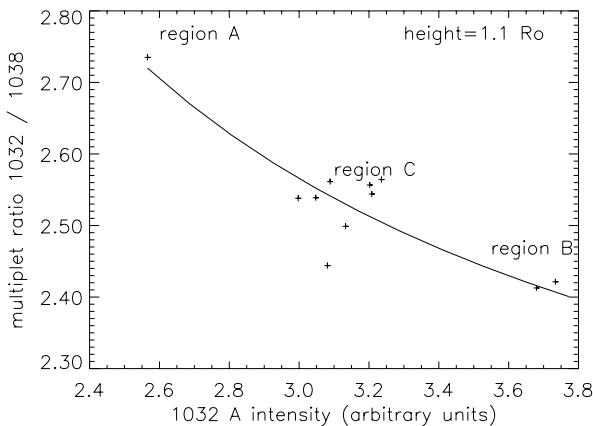

Fig. 14.— Test of the hypothesis that the weaker plumes in region C are of the same nature as the plume B, but with a smaller line-of-sight extent. The full line is a theoretical prediction. The points are the observations.

10.2. Plume geometries

As indicated in the Introduction, DeForest et al. (1997, 2001a) have claimed to observe continuity between some EIT plumes and white light plumes observed out to much greater distances. Furthermore, it is claimed that the observed plumes from EIT connect with the solar surface at high latitudes in polar holes, definitely inside the limb, where distinctive bright points or small magnetic regions are to be seen. Such plumes are often seen to rotate visibly with the Sun. At first sight, these observations might appear to be inconsistent with our present interpretation.

For the present work, we have tried to analyse the line shifts and widths. Widths are found to be slightly smaller in plumes than in interplume regions, consistent with previous observations (Hassler et al. 1997). However, no significant line shifts can be detected, also in accord with earlier workers (Wilhelm et al. 1998). If some plumes have a net inclination towards or away from the observer, we would expect to see line shifts, taking into account our high derived outflow velocities. Our raster data covered a duration of some 14 hours moving progressively out towards larger radial distances. Over this period of time, we might expect to see the effect of solar rotation in some of the plumes. However, none is detectable in Fig 7, where the time delay between the traces for 1.05 and 1.3 $R_\odot$ amounts to 10 hours.

These discrepancies have lead us to propose that XUV plumes, visible in EIT data, are of two distinct types. Those studied in the present paper are the more common. They consist of a line-of-sight alignment of structures over a considerable distance, perhaps some 0.5 $R_\odot$. Each has contributions that are in general distributed in front and behind the plane of the true limb. As such, they show no lateral rotation and no net Doppler shift. Their lifetime is limited by solar rotation to a period of visibility of a few days. We are unable to say whether these are due to the alignment of a number of cylindrical structures (see DeForest et al. (2001b)) or to a more curtain-like structure. The second type consists of a radial cylindrical structure, originating at some enhanced magnetic feature on the disk. Such plumes are rarer but generally brighter and more prominent. They show rotation and are seen both in front and behind the solar limb, with the appropriate rotation sense. Examination of EIT movies at 171 Å tends to confirm the existence of these two types of plume.

The present measurements of outflow velocity and intensity suggest that our plumes may merge with the interplume material at some height between 1.5 and 2.5 $R_\odot$. The JOP 002 observing sequence reported here included also a coordinated

12

sequence of observations from the UVCS instrument at higher altitudes. These data are currently being analysed for plumes, in an effort to answer these and related questions (E. Antonucci private communication).

10.3. Errors and assumptions

We have considered in which areas the assumptions that are made and the errors introduced might raise doubts regarding our conclusions. These uncertainties include the need to adopt standard generic coronal hole densities, residual errors in the stray light correction, the disk brightness and line profile adopted for the photo-excitation source, the assumed coronal thermal Doppler profile and the assumption of the absence of plumes in the selected interplume region B. Realistic values of such errors can of course modify some of the numbers quoted in our results. However, we can find no way in which such errors can invalidate the basic results that the flow rate is higher in the plume than the interplume region, and that this difference decreases with height, tending to merge at some height above our observational limit of 1.35 $R_\odot$.

As has already been stated, almost all of the results are derived from relative intensity measurements. The only absolute intensity that has been used relates to the disk brightness in oxygen VI, used to calculate the photo-excitation efficiency, important for the Doppler dimming. These values, derived from SUMER observations by Curdt, et al. (2001) could have errors of up to 30%. The effect of such an error would be the same as that of using density profiles that were 30% different, since it is the balance between impact and photo-excitation that determines the multiplet ratios observed. Such differences would not alter our basic conclusions.

10.4. Contribution to the solar wind flux

The proton outflow rate for the high-latitude fast wind observed during the solar minimum from Ulysses (McComas et al. 2000) is 2.05 10^8 proton/cm^2/s at 1 A.U. To scale this to the solar surface at the polar coronal hole, it must be multiplied by $(1 A.U./R_\odot)^2 = 46253$ and by a non-radial expansion factor of 4.9 (Munro and Jackson 1977), to give a coronal base mean outflow rate of 4.6

10^{13} proton/cm^2/s. This can be compared with the rates determined from our present derived velocities. For the interplume region, our density and velocity are equivalent to a value of 2.5 10^{13} proton/cm^2/s. For the plume region B, our result for $F = 1$ at a distance of 1.1 $R_\odot$ corresponds to a flow rate of 7.6 10^{13} proton/cm^2/s locally. From this, we can therefore deduce that the plumes occupy about one third of the surface of the coronal hole at this height and contribute to about one half of the total fast solar wind flux.

It is now possible to reconsider the interpretation of David et al. (1998) who measured the electron temperature as a function of height in this region, through the ratio of the oxygen VI 1032 Å plus 1038 Å multiplet to the XUV 173 Å line from the 2p-3d transition. For instrumental reasons it was necessary to integrate over the plume and interplume regions. The present work shows that both regions contribute equally to the solar wind flux and that, since the brightness contrast is only a factor of 1.4 at 1.1 $R_\odot$, there is no anomalous weighting in the observation. The result, that the electron temperature never exceeds about 1.0 MK therefore remains valid. This measured temperature is in conflict with the "freezing-in" temperatures observed at 1 A.U. of some 1.2 MK or higher (see discussion by Esser and Edgar (2000)). It therefore remains to understand whether the measured freezing-in temperatures are due to errors in the ionisation balance theory used, or to unknown processes occurring in the intervening interplanetary region.

REFERENCES

Antonucci, E., Dodero, M. A. and Giordano, S., 2000, Sol. Phys., 197, 115

Curdt, W., et al., 2001, A&A, 375, 591

David, C., Gabriel, A. H., Bely-Dubau, F., 1997, 5th SOHO Workshop, ESA SP404, p.313

David, C., Gabriel, A. H., Bely-Dubau, F., Fludra, A., Lemaire, P. and Wilhelm, K, 1998, A&A, 336, L90

DeForest, C. E., Hoeksema, J. E., Gurman, J. B., Thompson, B. J., Plunkett, S. P.,Howard, R., Harrison, R. C. and Hassler, D. M., 1997, Sol. Phys., 175, 393

DeForest, C. E., Plunkett, S. P., and Adrews, M. D., 2001a, ApJ, 546, 569

DeForest, C. E., Lamy, P. L. and Llebaria, A., 2001b, ApJ, 560, 490

Dodero, M. A., Antonucci, E., Giordano, S. and Martin, R., 1998, Sol. Phys., 183, 77

Doschek, G. A., et al., 1997, ApJ, 482, L109

Esser, R. and Edgar, R., 2000, ApJ, 532, L71

Gabriel, A. H., Bely-Dubau, F. and David, C., 2002, ESA SP477, p. 343

Giordano, S., Antonucci, E., Noci, G., Romoli, M, Kohl, J. L., 2000, ApJ, 531, L79

Hassler, D. M., Wilhelm, K., Lemaire, P. and Schühle, 1997, Sol. Phys., 175, 375

Koutchmy, S., 1994, Adv. in Space Res., 14, 29

Li, X., Habbal, S. R., Kohl, J. L. and Noci, G., 1998, ApJ, 501, L133

McComas, D. J., et al., 2000, J. Geophys. Res., 105, 10419

Munro, R. H. and Jackson, B. V., 1977, ApJ, 213, 847

Noci, G., Kohl, J. L. and Withbroe, G. L., 1987, ApJ, 315, 706

Patsourakos, S. and Vial, J.-C., 2000, A&A, 359, L1

Raouafi, N.-E., Sahal-Bréchot, S., Lemaire, P. and Bommier, V., 2002, A&A, 390, 691

Vial, J.-C, Lemaire, P., Artzner, G. and Gouttebroze, P., 1980, Sol. Phys., 68, 187

Wilhelm, K., Marsch, E., Dwivedi, B. N., Hassler, D. M., Lemaire, P., Gabriel, A. H. and Huber, M. C. D., 1998, ApJ, 500, 1023

Wurz, P. and Gabriel, A. H., 1999, 8th SOHO Workshop, ESA SP446, P.87

Zhang, H. L., Sampson, D. H. and Fontes, C. J., 1990, Atomic and Nuclear Data Tables, 44, 31
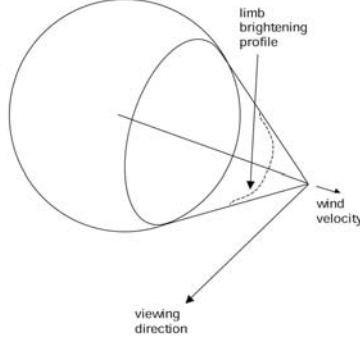
A. Appendix - Doppler dimming

Fig. 15.— Geometry of the Doppler dimming computation.

Since the presentation of the basic Doppler dimming technique for application to the oxygen VI multiplet by Noci et al. (1987), several users have refined and adapted the method of application (Dodero et al. 1998; Li et al., 1998; Patsourakos and Vial 2000; Gabriel et al. 2002). In the present paper, we follow the basic theory presented by Noci et al. (1987) but with certain changes. Some of these derive from an improved knowledge of the basic physical parameters used, some are due to the different geometrical domain to which the theory is being applied here and another represents a significant effect which was neglected in the original presentation. Fig 15 shows the basic geometry of the resonance scattering or photoexcitation process. As for the majority of workers applying this theory, we treat only the region of the line-of sight which is closest to the Sun. That is to say that we do not perform a true integration along the entire line of sight. This has been shown to be unnecessary, since the rapid fall-off of density with radial distance implies that almost the entire contribution comes from this region.

The photo-excitation rate per oxygen VI ion, ϕ, used in equation 3, can be expressed using atomic units in the form

$$\phi = \frac{32\pi^3}{\chi^2} a_0{}^3 f \int B \int L_\lambda L_\lambda' d\lambda d\omega, \tag{A1}$$

where L_λ and L_λ' are the emission and absorption profiles, normalised so that $\int L_\lambda d\lambda = 1$, B is the brightness of the solar disk, f is the oscillator strength of the transition, χ is the excitation energy in Rydbergs and the integral is over wavelength and solid angle of the illuminating disk flux. The integral over wavelength

$$D = \int L_\lambda L_\lambda' d\lambda \tag{A2}$$

is the Doppler dimming factor responsible for the dependence of ϕ on the outflow velocity v. Fig 16 shows the results obtained for the multiplet intensity ratio at two radial distances 1.1 and 1.3 $R_\odot$, for a range of electron densities.

The particular features of our dimming model can be listed:

- the use of more recent theory for the electron impact excitation of the oxygen VI levels (Zhang et al. 1990). This has been inserted in the model in the form of a modified value of the effective "gbar" for the excitation.

- the use of more recent values for the observed disk intensity of the oxygen VI lines (Curdt, et al. 2001).

- an improved observational figure for the wavelength interval between the carbon II and oxygen VI lines (Curdt, et al. 2001).

15

- we neglect the possibility of different ion Doppler widths in the parallel and transverse directions, (unimportant at our smaller radial distances).

- we correct for the small departure from isotropic re-emission for the 1032 Å line, using an empirical formula that we have fitted to numerical results supplied by D. Spadaro (private communication). The photo-excited emission for this line only is multiplied by $(7 + (R_\odot/R)^2)/8 - 0.012$

- the inclusion of a realistic limb-brightening function for the oxygen VI disk pumping source.

This last point is quite important. At all radial distances it has the effect of increasing the total disk flux by a factor of 2 or more. However, the geometrical distribution itself has a more important effect, since this increased flux comes at angles for which the dimming effect is less efficient. This means that a higher flow velocity is required to produce the same dimming effect, so that the velocity at which the multiplet ratio drops to 2.0 is increased from 100 km/s to some 130 km/s at moderate radial distances. The effect becomes even more important at the closer radial distances used by SUMER, so that at 1.1 $R_\odot$, a multiplet ratio of 2 requires a flow velocity of 165 km/s. This is based upon a theoretical limb brightening of $1/cos\theta$, which we show here is close to the observed value.

Table 1 shows a comparison of various input parameters as used by different authors. A further verification of the intensity and profile of the oxygen VI disk radiation can by obtained from Vial et al. (1980), using data from OSO-8. They obtain 300 ± 115 erg/sterad/cm^2/s for the 1032 Å line, with a FWHM of 0.18 Å, which are fully consistent with the values used in the present work.
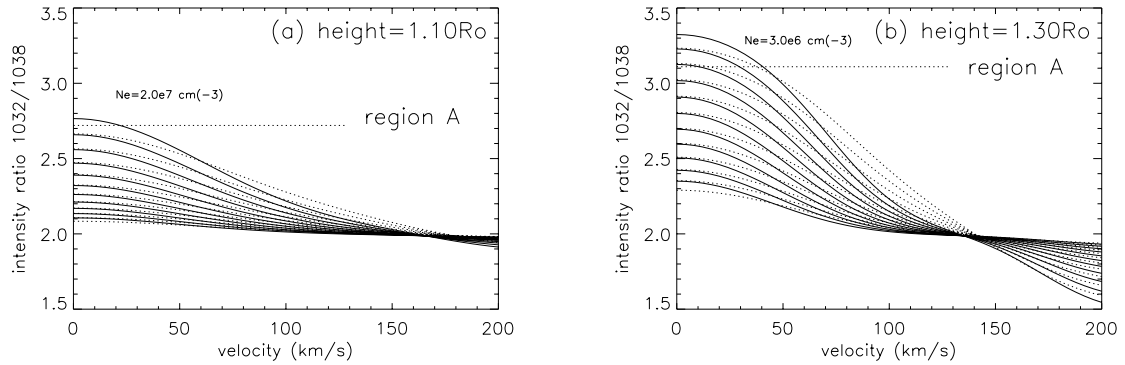

Fig. 16.— Results of the Doppler dimming calculations, showing how the multiplet intensity ratio depends upon the outflow velocity and the local density, for values of the radial distance of 1.1 $R_\odot$ and 1.3 $R_\odot$. The indicated density refers to the upper curve in each graph. The lower curves represent successive increases in density in steps of factor $10^{0.1}$. The full curves are for an ion Doppler temperature T_i of 1 MK. The dotted curves show the effect of $T_i=2$ MK.

16

TABLE 1

DOPPLER DIMMING INPUT PARAMETERS ADOPTED BY DIFFERENT AUTHORS

Parameter	Noci et al. (1987)	Li et al., (1998)	Dodero et al. (1998)	Patsourakos and Vial (2000)	this work
Disk intensities (ergs/sterad/cm^2/s)					
O VI 1032 Å	305	305	248	335	333.5
O VI 1038 Å	152	152	118	186	159.5
C II 1037.6 Å	52	52	44.8	71.3	57.7
C II 1037 Å			35.9		49.7
Limb brightening applied	no	no	no	intensity x 2	full geometry
FWHM disk O VI (Å)	0.168	0.166	0.212	0.233/0.208	0.168
FWHM C II (Å)	0.12	0.116	0.152	0.268	0.12
"gbar" for O VI excitation	1.36	1.36	1.36	1.36	1.20
λ interval C II - O VI (Å)	0.59	0.59	0.59	0.59	0.64